Breast-region segmentation in MRI using chest region atlas and SVM

Aida FOOLADIVANDA[1,*], **Shahriar BARADARAN SHOKOUHI**[1], **Nasrin AHMADINEJAD**[2]

[1]Department of Electrical Engineering, Iran University of Science and Technology, Tehran, Iran

[2]Advanced Diagnostic and Interventional Radiology Research Center, Tehran University of Medical Science, Tehran, Iran

Abstract: An important step for computerized analysis of breast magnetic resonance imaging (MRI) is segmentation of the breast region. Due to the similar signal intensity of fibroglandular tissue and the chest wall, the segmentation process is difficult for breasts with fibroglandular tissue connected to the chest wall. In order to overcome this challenge, a new framework is presented that relies on a chest region atlas. The proposed method first detects the approximated breast–chest wall boundary using an intensity-based operation. A support vector machine (SVM) then determines the connectivity of fibroglandular tissue to the chest wall by the extracted features from the obtained breast–chest wall boundary. Finally, the obtained breast–chest wall boundary is accurately refined using the geometric shape of the chest region, which is obtained by an atlas-based segmentation method. The proposed method is validated using a dataset of 5964 breast MRI images from 126 women. The Dice similarity coefficient (DSC), total overlap (TO), false negative (FN), and false positive (FP) values are calculated to measure the similarity between automatic and manual segmentation results. Our method achieves DSC, TO, FN, and FP values of 96.46%, 96.41%, 3.59%, and 3.51%, respectively. The results prove the effectiveness of the presented algorithm for breasts with different sizes, shapes, and density patterns.

Key words: Breast magnetic resonance imaging, breast segmentation, support vector machine, atlas-based segmentation, chest region atlas

1. Introduction

Despite significant progress in the early diagnosis and treatment of breast cancer, this type of cancer is still considered to be one of the most deadly maladies among women [1]. Breast magnetic resonance imaging (MRI) is an invaluable modality for high-risk screening, cancer staging, and diagnosis [2]. Computerized methods are increasingly used for detection of breast lesions [3] and density assessment [4] in MRI. An important step to perform an automatic analysis is segmentation of the whole breast from other parts of the captured image. Automatic breast segmentation can be done in a computer-aided diagnosis system to decrease the false positive rate by removing unwanted parts in the processed image. Furthermore, breast segmentation is necessary to calculate the total breast volume for density estimation, which is an important metric for assessing cancer risk [5].

T1-weighted nonfat-suppressed MRI images are usually included in all typical clinical breast MRI imaging protocols and are used for breast segmentation and density estimation. In this type of imaging technique, fat appears as the brightest and air (background) as the darkest signal. Fibroglandular tissue, tumors, and the

---

*Correspondence: a_fooladivanda@iust.ac.ir

chest wall appear as moderate signals with similar signal intensity [6]. Hence, for challenging cases where a part of the fibroglandular tissue is connected to the chest wall and there is no fat along the anterior side of the chest wall, breast segmentation is a difficult task. Figure 1 shows axial breast MRI images for four different cases. Figures 1a and 1b present some sample breast images with fat along the anterior of the chest wall. Due to the presence of the fat along the anterior of the chest wall, there are visible contrasts between the breast region and chest wall. Figures 1c and 1d provide extra breast images with fibroglandular tissue connected to the chest wall.
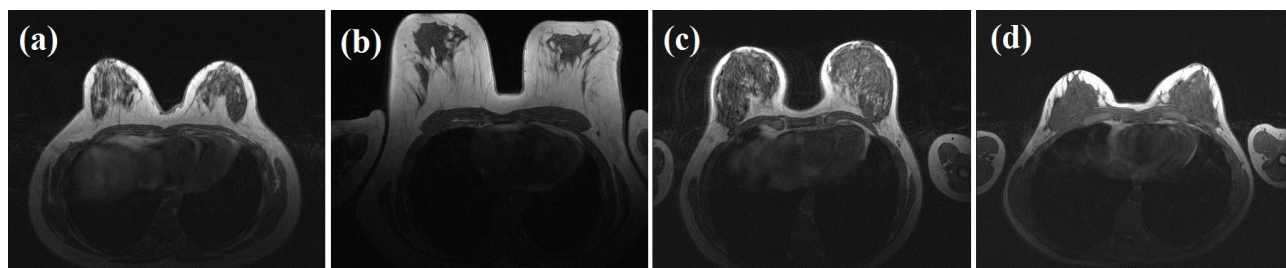

Figure 1. Axial breast MR images for four different cases: a, b) sample images with fat along the anterior of the chest wall; c, d) sample images with fibroglandular tissue connected to the chest wall.

Most of the reported algorithms in the literature have delineated the breast boundary manually or have presented semiautomatic segmentation approaches that need some operator interferences [4,5]. These methods are time-consuming and the results of segmentation can be variable due to their dependency on the operator's personal decision. Some studies proposed automated approaches for breast segmentation. Ertas et al. [7] presented a breast segmentation method using two kinds of cellular neural networks; one is for thresholding and another for removing small objects and smoothing sharp corners. In another work [8], 3D bias-corrected fuzzy c-means clustering and morphological operations were used to determine the breast region. Hyton et al. [9] applied a morphological opening operator iteratively with increasing scales of structure elements until eliminating the breast region and keeping the remaining part as an initial approximation for location of the breast–chest wall boundary. They employed a graph search algorithm to find the most likely boundary, which is located close to the approximated location of the chest wall boundary with a similar shape and an alteration in signal intensity. Yao et al. [10] employed B-spline fitting and an active contour model to locate the breast–air boundary. Following that, the initial breast–chest wall boundary is achieved by connecting three landmarks, which are automatically detected by the breast–air profile. This boundary is amended using a muscle-slab model that is a curved slab with different thicknesses at distinctive locations. Some studies also used the thresholding and morphological operations for breast isolation [11–13]. Giannini et al. [14] segmented the breast region from the MRI images by sign of gradients. Wu et al. [15], Lin et al. [16], and Wang et al. [17] proposed edge-based methods for detecting the breast–chest wall boundary by relying on the Canny edge detection method and a Hessian-based filter. Jiang et al. [18] and Rosado-Toro et al. [19] presented variants of the dynamic programming approach to segment the whole breast. All of the mentioned approaches relied on the visible contrast between the breast region and the chest wall and their processes are dependent on the presence of the fat along the anterior of the chest wall. In this regards, these approaches may fail to segment breasts with fibroglandular tissue connected to the chest wall due to the similar signal intensity of fibroglandular tissue and the chest wall and no visible contrast between them. Only Milenković et al. [20] considered the breast segmentation issue for challenging cases where a part of the fibroglandular tissue is connected to the chest wall and suggested a breast segmentation method independent from the contrast between the breast region and chest wall. In their method,

nonvisible transitions between different tissues with similar intensities are detected by applying a tunable Gabor filter where its parameters are calculated based on the local MRI image characteristics.

Atlas-based methods are often employed when there is no well-defined relationship between pixels' intensities and regions. In this procedure, the segmentation process is performed by relying on the geometrical constraints and spatial information [21]. To date, only a few studies have employed atlas-based methods for breast segmentation in MRI [22–24]. Gubern-Merida et al. [22] defined a probabilistic atlas in a Bayesian framework for separating different structures in breast MRIs. Gallego-Ortiz et al. [23] employed a Poisson surface reconstruction algorithm to reconstruct the breast surface from the obtained points by a phase congruency filter. The breast surface is purified using a probabilistic breast atlas. Khalvati et al. [24] use clustered probabilistic atlases for breast segmentation. These approaches utilize a breast template to construct the atlas set. To define a general breast template for separating different breasts is a difficult task because of the great variability in shapes and tissues of breasts. In axial breast MRI, the chest region is observed at similar locations with similar signal intensity and shape. Thus, separating the breast region using a chest region atlas can generate more accurate result. Recently, Fooladivanda et al. [25] proposed a robust atlas-based breast segmentation method by relying on the chest wall template. In this paper, an atlas-based technique using the chest region template is proposed to segment the breast region in MRI.

Unlike many literature methods proposed for breast segmentation that rely on the high contrast boundaries of breasts, we present a robust method that is applicable for cases with high contrast boundaries as well as challenging cases where a part of the fibroglandular tissue is connected to the chest wall with no visible contrast between them. Our breast-region segmentation method is a combination of both atlas-based and intensity-based techniques. Most of the atlas-based breast segmentation techniques employ the breast template, while we propose a novel method that can detect the breast region using a chest region atlas. For breasts with high contrast boundaries, our approach works with intensity-based operations. Likewise, for challenging cases, the results from the intensity-based method are refined using the geometric shape of the chest region, which is obtained by atlas-based segmentation method. The geometric shape of the chest region is used for the first time in order to solve the breast segmentation problem. A classification algorithm based on a support vector machine (SVM) is presented to determine the processing methods mentioned above. The classification step guarantees that the atlas-based segmentation method is applied only to breasts with fibroglandular tissue connected to the chest wall to decrease the computational time and complexity.

Our paper is organized as follows. Section 2 consists of the two main steps including description of the clinical breast MRI scans and explanation of the proposed breast segmentation method. Section 3 provides the experimental results and discusses the outcomes of this research. Finally, conclusions are summarized in Section 4.

2. Materials and methods

2.1. Data acquisition

The 3D bilateral axial breast MRI images of 126 women (22–68 years old; mean = 44 years) have been used in this study. The cases were collected from the Noor Medical Imaging Center and Valiasr MRI Center in Tehran for the duration of 2012 to 2016. This study was approved by the institutional review board and informed consent was waived. The breast MRI scanning process is performed in the prone position with a dedicated four-channel breast coil (CP Breast Array, Siemens) on a 1.5-T Siemens scanner (Magnetom, Symphony) or with a dedicated eight-channel breast coil on a 1.5-T Signa HDXT scanner (GE, Milwaukee, WI, USA). In

both scanners, the precontrast T1-weighted nonfat-suppressed breast volumes are acquired. Table 1 presents the clinical imaging parameters of our dataset. The prepared dataset contains data from 58 healthy women with a genetically high risk for breast cancer and 68 women with biopsy-proven lesions (49 benign and 23 malignant lesions). Our automatic segmentation algorithm is validated with manual segmentation. The manual segmentation of the breast region is performed by a professional radiologist with at least 6 years of experience in reading breast MRI images in a dedicated breast MRI annotation environment [26]. The dataset includes all four groups of the American College of Radiology (ACR) Breast Imaging-Reporting and Data System (BI-RADS) breast density ranges (I: <25%; II: 25%–50%; III: 51%–75%; IV: >75%). An experienced radiologist determines the BI-RADS categories visually.

Table 1. The clinical imaging parameters for the captured breast MRI images.

Scanner	Siemens 1.5 T	GE Signa HDXT 1.5T
Dimensions (pixels)	$448 \times 448 \times 56$, $320 \times 320 \times 56$	$512 \times 512 \times 30$
Field of view (mm)	378–424	280–330
Flip angle (°)	14	90
TR (ms)	4.7–4.8	600
Slice thickness (mm)	2–2.8	5
TE (ms)	1.4–1.5	12

2.2. The breast segmentation scheme

The flowchart of the proposed breast segmentation algorithm is shown in Figure 2. First, an approximated binary mask is achieved by local thresholding and morphological operation. Subsequently, an edge detector is applied and approximated boundaries of the breast region are specified using several landmark points determined on the edge map. In this step, an accurate breast–air boundary can be found, but the obtained boundary between breast and chest wall is an approximated result. The SVM then classifies breasts based on the obtained breast–chest wall boundary to determine breasts that need atlas-based refinement. This process is continued until segmentation of all slices of the 3D MRI data. The step-by-step procedures of our proposed breast segmentation approach are explained in the following subsections in detail.
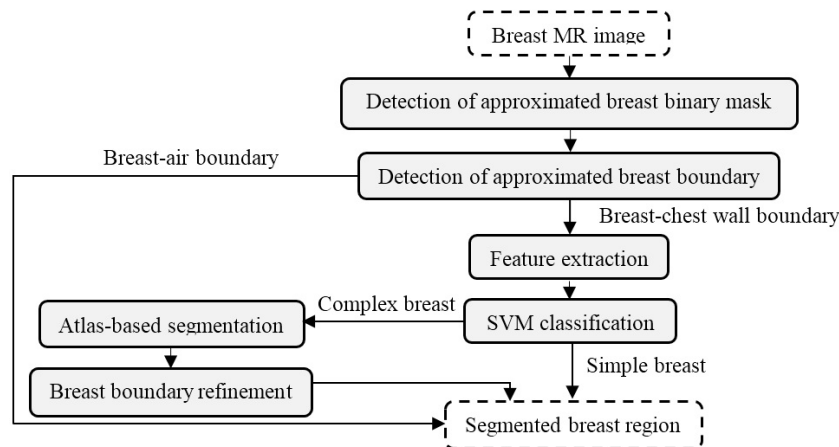

Figure 2. Flowchart of the proposed breast segmentation algorithm.

2.2.1. Detection of approximated breast binary mask

First, intrapatient signal intensity variability is corrected using the multiplicative intrinsic component optimization (MICO) algorithm [27]. The MICO bias field correction algorithm is an energy minimization method for correcting image inhomogeneities in MRI images. Moreover, interpatient signal intensity variability can affect the segmentation results, especially when the intensity-based operation is utilized. Hence, we have compensated the difference between signal intensities of different scans by normalizing the image intensity values according to the mean fatty tissue value [22].

In this work, Sauvola's local thresholding algorithm is used, which was originally presented for document images [28]. The different values of the local window size are examined and a window size of 41×41 is found as an optimum value for the breast MRI images in our database. The results of the processing steps to detect the approximated breast binary mask are shown in Figure 3. Figure 3a shows a sample breast MRI image and Figure 3b shows the result after thresholding.
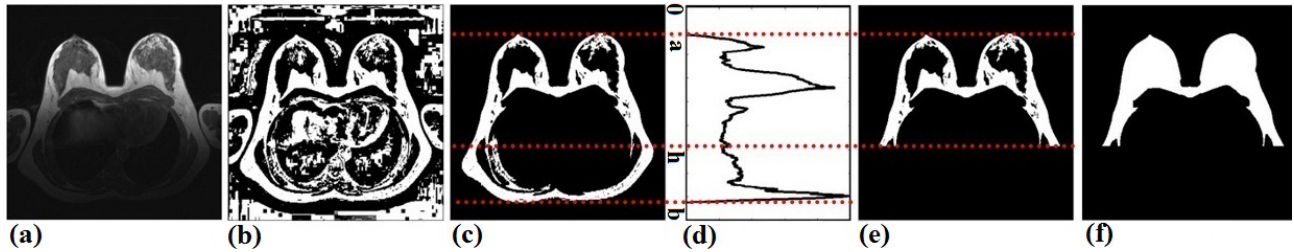

Figure 3. The process of finding an approximated breast binary mask: a) the original image, b) the binary image, c) the binarized image after connected-component labeling, d) the horizontal projection of the image, e) the defined breast area by horizontal projection, and f) the final breast binary mask after morphological operation.

The achieved binary image contains the breast area and unwanted objects such as background noise, lung, heart, and in some cases even arms. The connected-component labeling operation [29] is applied to remove unwanted objects. The area of each individual object is computed and the object with the largest area in the binary image is selected. The result of the labeling operation is shown in Figure 3c. Horizontal projection [30] is applied for removing extra tissues in the binary image, which is defined as

$$H\left(y\right) = \sum_{x=1}^{M} I\left(x, y\right), \tag{1}$$

where $I(xy)$ refers to a binary image with size $M \times N$ and (x, y) shows the coordinates of each pixel. The horizontal projection of a binary image is plotted in Figure 3d. A simple experimental equation is defined to separate the breast region based on horizontal projection as:

$$h = a + \frac{2}{3}\left(b - a\right), \tag{2}$$

where a and b are the first and last nonzero values of the horizontal projection. Parameter a is the first row in the binary image in which the breast region begins, and parameter b is the end row where that body (white region) is observed. An area is defined between rows a and h as the initial breast region, which is presented in Figure 3e. Then a hole-filling operation (8 connectivity) [31] is applied to the binary image to erase fibroglandular tissue and tumors in the breast area. The discontinuities in the breast boundary are eliminated

using the morphological closing operator with a circular structuring element of radius 4 mm. Figure 3f shows the final breast binary mask after morphological operations.

2.2.2. Detection of approximated breast boundary

In this stage, the boundary of the breast binary mask is extracted by a Sobel edge detector and the edge map is generated. The edge map of the breast binary mask, which is achieved in Figure 3, is presented in Figure 4. The breast boundary is determined using three body landmarks (p, q, and n) shown in Figure 4a. First, points p and q are detected on the edge map with minimum and maximum x-coordinates, respectively. Then the edge map image is divided into two parts using a vertical line that is located in the middle of points p and q. Point n is the second crossing point between the vertical line and edge map, located on the breast-chest wall boundary. In the next step, a horizontal truncation line is delineated through the point placed 15 mm below point n, which places it on the anterior boundary of the sternum in the edge map image (Figure 4b). Based on Change's work [32] and the advice of two experienced radiologists, a separation threshold of 15 mm is selected. The boundaries at the top of this line are considered as the breast boundaries (Figure 4c). This process divides the edge map into two parts. The one for which the landmark n is its member is selected as the breast–chest wall boundary and the other one is the breast–air boundary.
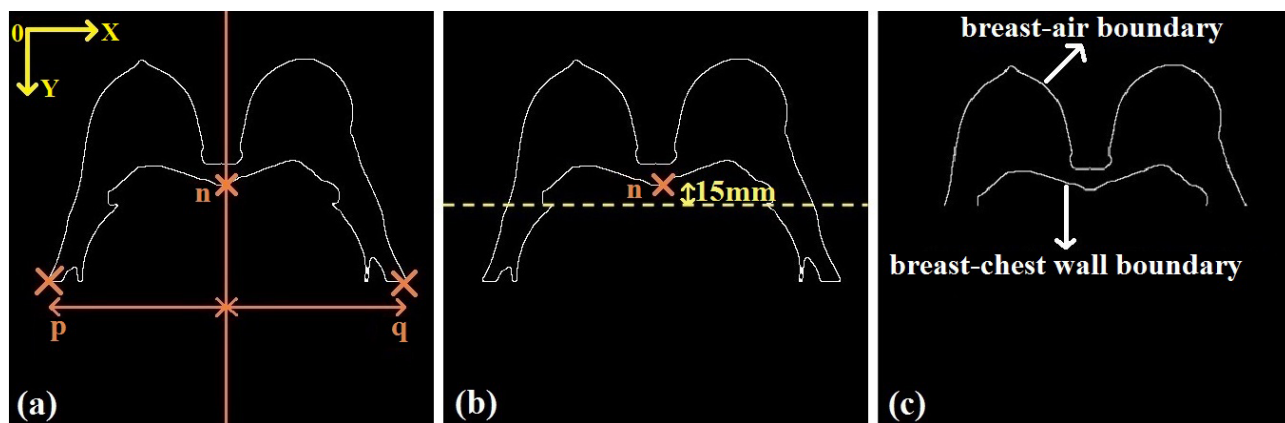

Figure 4. Finding the approximated boundaries of the breast: a) the edge map of the breast region with three body landmarks and a vertical line to determine point n, b) the position of horizontal truncation line, and c) the breast boundaries.

Because of high contrast intensity between breast tissue and air, the obtained breast–air boundary in this step is an accurate boundary. However, the obtained breast–chest wall boundary requires applying extra processing steps, which include classification based on extracted features from the breast–chest wall boundary and atlas-based refinement.

2.2.3. Feature extraction

The obtained breast–chest wall boundaries in the previous subsection are classified into two classes based on the connectivity of fibroglandular tissue to the chest wall. The two classes are simple and complex breasts. The breasts with high contrast boundaries are called simple breasts and breasts with fibroglandular tissue connected to the chest wall are called complex breasts. Due to the high contrast intensity between fat tissue and the chest wall in simple breasts, the achieved breast–chest wall boundary gives a precise result. However, the boundary detection algorithm requires extra processing steps in order to detect accurate breast–chest wall boundaries of

complex breasts. The approximated breast–chest wall boundaries are illustrated in Figure 5 for simple and complex breasts. As can be seen in Figure 5, the approximated breast–chest wall boundaries of simple and complex breasts have different shapes and attributes. The boundaries of simple breasts have almost a concave shape with smooth variation. In contrast, the boundaries of complex breasts have complicated shapes with large variation, especially in the y-coordinate. The extracted features from the obtained breast–chest wall boundaries defined below are used to distinguish simple and complex breasts.
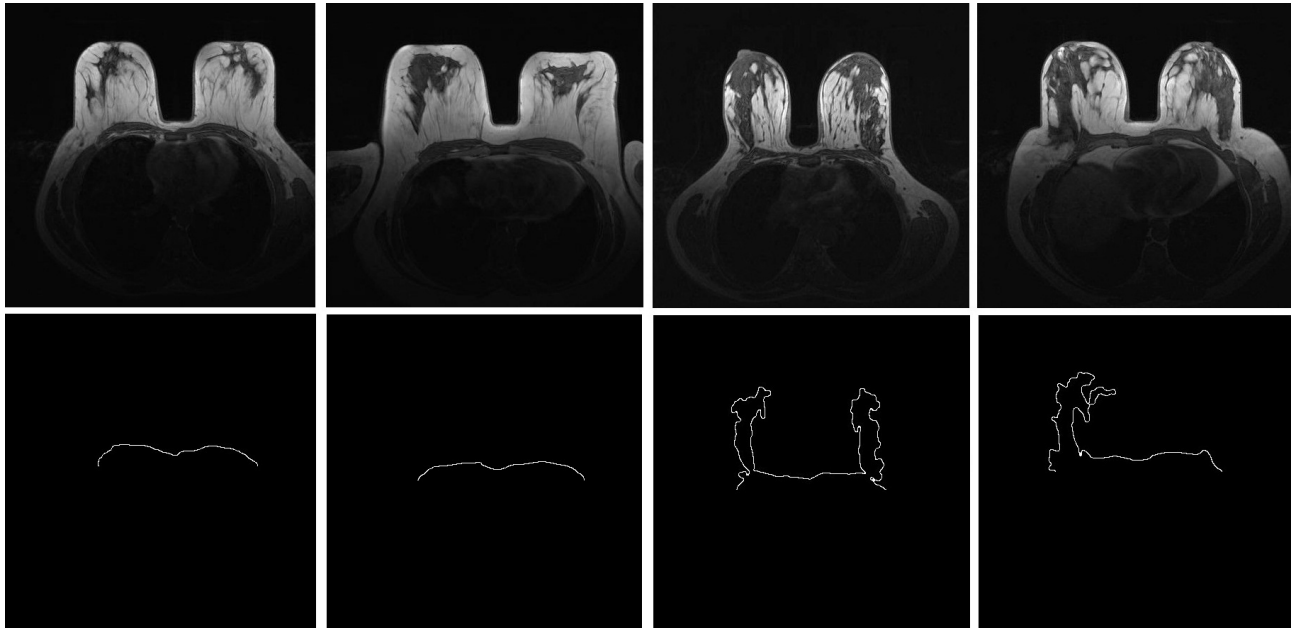

Figure 5. Illustration of the breast–chest wall boundary for simple (first and second columns) and complex (third and fourth columns) breasts. First and second rows present original images and approximated breast–chest wall boundaries, respectively.

1. Sum of local variations (SLV):

$$SLV = \frac{\sum_{i=2}^{Z} |C_y(i) - C_y(i-1)|}{N - M}, \tag{3}$$

2. Length of boundary (LB):

$$LB = \frac{Z}{N - M}, \tag{4}$$

3. Eccentricity of boundary points (EBP):

$$EBP = \frac{Q - P}{N - M}, \tag{5}$$

4. Standard deviation of y-coordinates (SDYC):

$$SDYC = std([C_y(1), \ldots, C_y(Z)]), \tag{6}$$

where Z is the number of the boundary points. $C_y(i)$ denotes the y-coordinate of the ith point on the boundary. P/Q and M/N denote the y-coordinates and x-coordinates of the first/last points of the boundary. The scaling normalization method is used to normalize the data where the resulting normalized features have zero mean and unit variance. In Figure 6, the scatterplot of a 4-dimensional feature vector is presented for some simple and complex breast samples. For better visualization of the distribution of the defined features, dimensions of the input data are decreased to two dimensions using a multidimensional scaling method. As can be seen in this figure, the defined features have different distributions for simple and complex breasts.
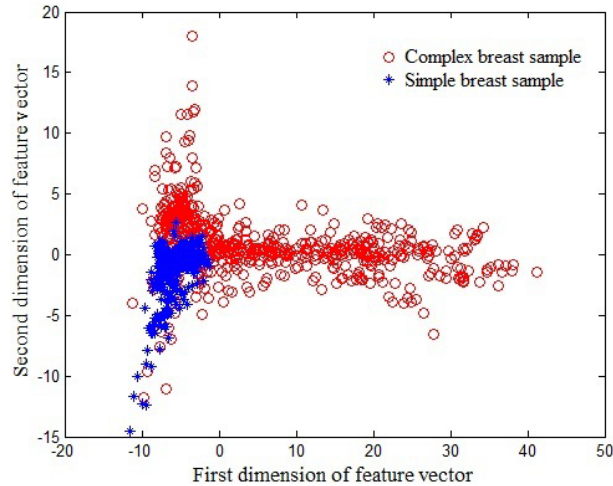

Figure 6. The scatterplot of a 4-dimensional feature vector is presented; dimensions of input data are decreased using a multidimensional scaling method to two dimensions.

2.2.4. SVM classification

In this work, a SVM is utilized to classify simple and complex breasts by relying on the extracted features from the breast–chest wall boundaries. The SVM is one of the most successful statistical learning methods. The significant characteristics of a SVM are high generalization ability, robustness to outliers, and absence of local minima [33]. This classifier finds an optimal separating hyperplane as the decision surface, which attempts to maximize its distance to the closest data point on either side of the surface. The SVM can linearly separate nonlinear data by mapping the data into a higher dimensional feature space using a kernel transformation function. In this paper, we evaluate the performance of the SVM with linear, polynomial, and Radial basis function (RBF) kernels.

2.2.5. Atlas-based segmentation

In this work, the interior boundary of the chest region is used to refine the obtained breast–chest wall boundary for complex breasts. We use Khalvati's atlas-based segmentation method [24] for detecting the chest region. In this method, the atlas images are divided into classes based on their pairwise similarities. Afterwards, each class of atlas images produces a probabilistic atlas. The optimum value for the number of probabilistic atlases is reported in Section 3.

There is high contrast intensity between the breast and air region, but the breast–chest wall boundary often has low contrast or even no boundary. If the entire image is used in atlas-based segmentation, the registration algorithm focuses on the breast–air boundary and there will not be good results near the chest

wall. Hence, all rows at the top of the landmark point n, which is obtained in Section 2.2.2, are excluded from the test and atlas images. This process is illustrated for an atlas image in Figure 7. Figure 7a shows a sample breast MRI image. The cut image and corresponding label image (the chest region is manually determined by the radiologist) are respectively shown in Figures 7b and 7c.
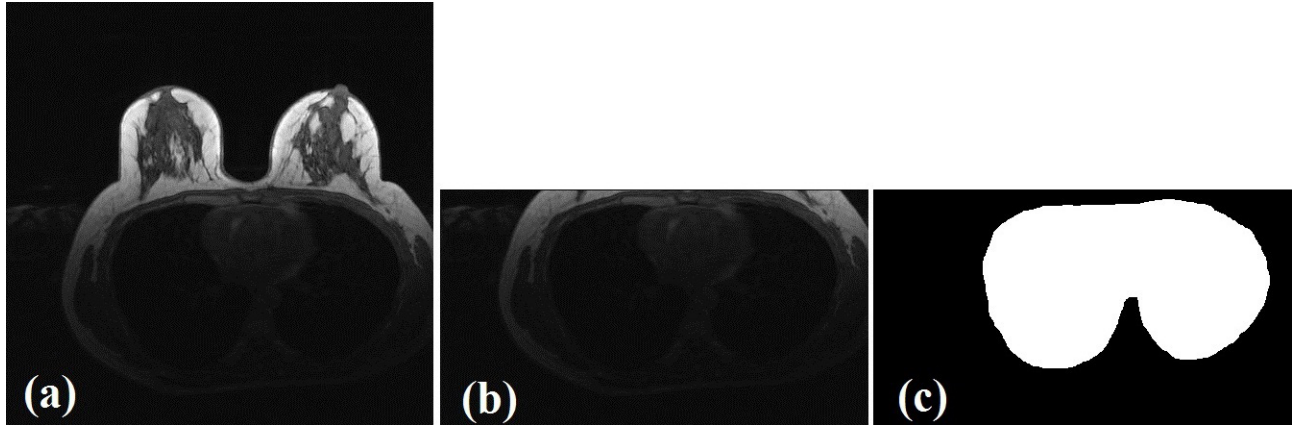

Figure 7. a) The original breast MRI image, b) the cut image, and c) the corresponding label.

In this study, an atlas-based segmentation method is applied to each slice to find the chest region. To follow the process of atlas construction, the entire atlas images are initially aligned using an affine registration. The match between any pair of atlas images is then computed based on a cross-correlation coefficient. For n atlas images, $n(n-1)/2$ similarity values are made that are inserted into a multidimensional scaling algorithm [34] to generate a 2D Euclidean distance map of all atlas images. The K-means algorithm clusters atlas images into N classes based on the distance map. The different values of N are tested to achieve the optimum value and the results are reported in Section 3. Each class includes several atlas images and their manual labels. Afterward, a group-wise registration aligns all of the atlas images in each class to a common reference image for creating the probabilistic atlas for each class. The probabilistic atlas and labeled images are computed as below [24]:

$$I_j^p(x) = \frac{1}{m_j} \sum_{k=1}^{m_j} I_j^k(x) \circ T_{I_j^k(x) \to I_j^R(x)}, \tag{7}$$

$$L_j^p(x) = \frac{1}{m_j} \sum_{k=1}^{m_j} L_j^k(x) \circ T_{I_j^k(x) \to I_j^R(x)}, \tag{8}$$

where m_j is the number of atlas images in class j. I_j^k and L_j^k are the kth atlas image and corresponding labeled image in class j. I_j^R is a common reference image. I_j^p and L_j^p are the probabilistic atlas image and a label for class j. T is a combination of global and local transformations. An affine transformation is applied to obtain the global adjustment and a nonrigid registration based on B-splines computes the local differences between the atlas and reference images. For matching the probabilistic atlas to the target image, the target image is initially aligned via affine registration and compared to the probabilistic atlas images for finding the most similar probabilistic atlas image that generates the maximum cross-correlation coefficient. Consequently, the selected atlas image is locally aligned with a target image via nonrigid registration. The achieved transformation is

applied to the corresponding labeled image to produce the chest region for the target image. The registration algorithm is implemented using the Medical Image Registration Toolbox [35].

2.2.6. Breast boundary refinement

For complex breasts, we extract the approximated breast–chest wall boundary and interior boundary of the chest region in Section 2.2.2 and Section 2.2.5, respectively. The pectoral muscle has a limited thickness in different locations. The maximum value of this thickness, t_{max}, is computed by averaging the maximum thickness values of the pectoral muscle for all images in the training set. The breast–chest wall boundary is located almost parallel to the interior boundary of the chest region. The vertical distance between each point of the approximated breast–chest wall boundary $\left(x_i^b, y_i^b\right)$ and equivalent point on the interior boundary of the chest region (x_i^c, y_i^c) is computed as r_i. In Section 2.2.2, the landmark point n on the breast–chest wall boundary has been found. The distance between this point and its equivalent point on the interior boundary of the chest region is computed as r'. This value is the vertical length of the sternum and is defined as a shift value. The breast–chest wall boundary for complex breasts can be refined as follows:

$$y_i^c - y_i^b = r_i, \qquad \text{for} \qquad i = 1, \ldots, Z \tag{9}$$

$$\begin{cases} \text{if } r_i < t_{max} \ \rightarrow y_i^{bnew} = y_i^b, \\ \text{if } r_i > t_{max} \ \rightarrow y_i^{bnew} = y_i^c - r', \end{cases} \tag{10}$$

where Z is the number of the approximated breast–chest wall boundary points. y_i^{bnew} is the refined breast–chest wall boundary. The distance between points of the breast boundary and the interior boundary of the chest region is calculated. If this distance is higher than t_{max}, the interior boundary of the chest region will be shifted and replaced by the breast boundary point. The refining process for a sample slice is shown in Figure 8. Figure 8a shows a sample breast MRI image. The approximated breast–chest wall boundary and the chest region boundary are presented for this sample breast image in Figure 8b. A zoom-in local portion of Figure 8b is shown in Figure 8c for better comprehension of $\mathbf{r_i}$ and $\mathbf{r'}$ values. The refined breast–chest wall boundary and all boundaries of the breast are shown in Figures 8d and 8e, respectively.

3. Results and discussion

To classify simple and complex breasts perfectly, we need to find the best SVM configuration. In general, for large databases, the input instances are divided into three equal-sized categories called training, validation, and testing; each category contains approximately 33% of the total input instances. To find the best architecture for the classifier, the average of 5 runs is computed [36,37]. In this paper, our prepared dataset, which contains the data of 126 cases, is partitioned into three groups. First, the classifier is trained using the training set and the best architecture is found by evaluating the accuracy on the validation set. The SVM-KM Toolbox [38] has been used in our work to implement the SVM classifier. Cost C and the kernel parameters are optimized. A linear SVM and nonlinear SVM with polynomial (kernel degree d between 2 and 5) and RBF (kernel scale γ between 0.001 and 5) kernels have been examined to choose the appropriate kernel with the best parameter. The performance of different configurations of the SVM is compared based on the area under the ROC curve (AUC) in Table 2. In this table, the average values of 5 runs are presented and the values in parentheses refer to the standard deviation. As can be seen in Table 2, the best performance from the SVM has been obtained
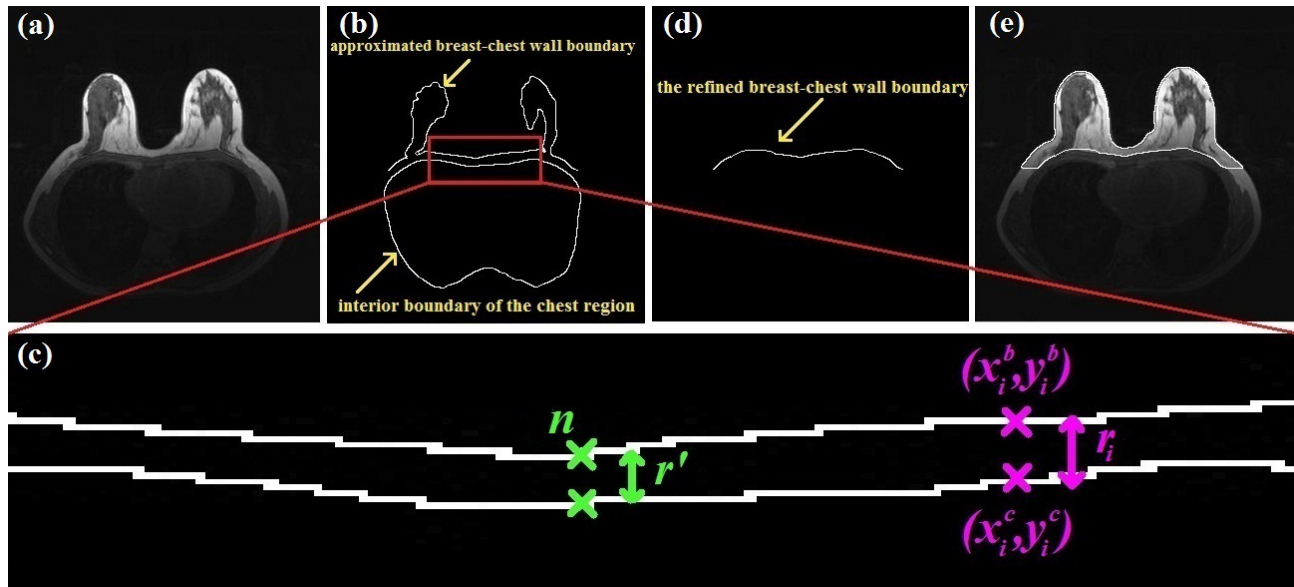
Figure 8. The refining process to find an accurate breast boundary: a) the original image, b) comparing the approximated breast–chest wall boundary with the chest region boundary, c) a zoom-in local portion of (b) for better comprehension of r_i and r' values, d, e) the refined breast–chest wall boundary.

by the RBF kernel with $\gamma = 0.005$. The range of cost parameter C is $\left[2^{-i}, 2^i\right]$, $i = 1, 2, \cdots, 10$. After finding the best configuration for the classifier with the aid of the validation set, the performance of the classifier is evaluated in terms of the testing set, which contains unseen patterns for the trained classifier. The performance of the classifier has been analyzed in terms of the accuracy, AUC, recall, precision, and f-measure and the results are reported on both the validation and testing sets in Table 3. A plot of true positive rate (TPR) with respect to false positive rate (FPR) with different decision thresholds has been considered as the ROC curve. Here, the probability of incorrect classification for a simple breast is defined as FPR, whereas TPR is computed as the probability of correct classification for a complex breast. In Figure 9, the ROC curves for the training, validation, and testing sets are shown. As can be seen in Table 3 and Figure 9, the performance of the SVM to classify simple and complex breasts on the unseen instances of the testing set is weaker than that based on the training and validation sets.

The accuracy of the SVM for classifying the simple and complex cases is 94.5%. If a simple or complex breast is incorrectly classified, the breast–air boundary will not be affected. However, it may produce inaccurate results for detecting the breast–chest wall boundary. If a simple case is wrongly classified as a complex case (FP responses), it does not affect the accuracy. Because only an atlas-based refinement is added to the processing stage and according to the shift value, the breast–chest wall boundary remains unchanged. For a complex case that is wrongly classified as a simple case (FN responses), the obtained breast–chest wall boundary in this step will be the final result and the atlas-based refinement step will be omitted. This causes small parts of the chest wall to be detected incorrectly as a part of the breast area, or an inability to detect small parts of the breast region. Precision and recall metrics correspond to the FP and FN responses, respectively. The high value of recall in Table 3 refers to the low value of the FN response in our results, i.e. a small number of complex cases are wrongly classified as simple cases.

The training set, which contains 42 cases or 33% of the total dataset, is employed for atlas construction.
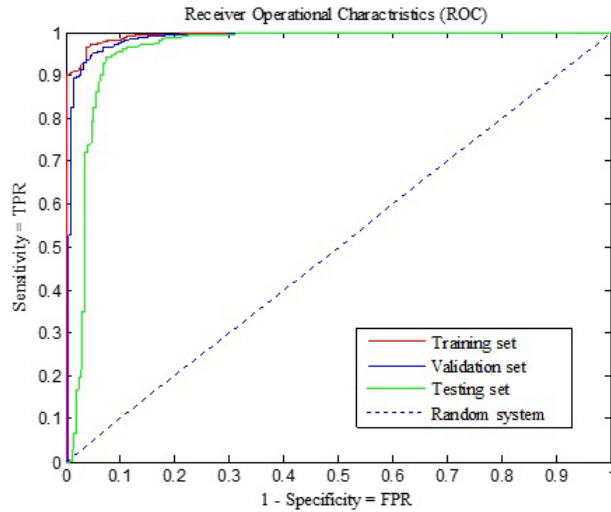
Figure 9. ROC plots of the classification step for the training, validation, and testing sets.

Table 2. Average values of AUC for different SVM configurations: mean (standard deviation).

SVM configuration	AUC
Linear	0.946 (0.024)
Polynomial (d = 2)	0.946 (0.031)
Polynomial (d = 3)	0.961 (0.024)
Polynomial (d = 4)	0.752 (0.034)
Polynomial (d = 5)	0.563 (0.027)
RBF ($\gamma = 0.001$)	0.981 (0.021)
RBF ($\gamma = 0.005$)	0.985 (0.023)
RBF ($\gamma = 0.01$)	0.972 (0.021)
RBF ($\gamma = 0.1$)	0.913 (0.034)
RBF ($\gamma = 0.5$)	0.88 (0.034)
RBF ($\gamma = 1$)	0.89 (0.036)
RBF ($\gamma = 5$)	0.929 (0.039)

Table 3. Results of the SVM to classify the simple and complex breasts.

Dataset	Precision (%)	Recall (%)	F-Measure (%)	Accuracy (%)	AUC
Validation	72.62	93.17	81.62	95.9	0.985
Testing	70.94	90.8	79.65	94.5	0.956

We randomly select 5 slices from each case to construct the atlas set. This means that 210 images are employed for atlas construction. Different numbers of atlas classes are investigated and the results are reported in Figure 10. The Pearson correlation coefficient (r) and mean DSC are presented for the validation set with respect to different numbers of atlas classes in Figures 10a and 10b, respectively. Three classes of probabilistic atlases yield the best results to segment the chest region.

The segmentation results for six breasts with different sizes, shapes, and densities are presented in Figure 11. Figures 11a and 11b display two simple cases with high contrast boundaries. Figures 11c–11f show the segmentation results in complex cases in which fibroglandular tissue is connected to the chest wall. In Figures 11c and 11d, the breast region is accurately segmented with the proposed algorithm. In Figure 11e, the automatic segmentation algorithm excludes a small part of the breast region incorrectly. In Figure 11f, a small part of the
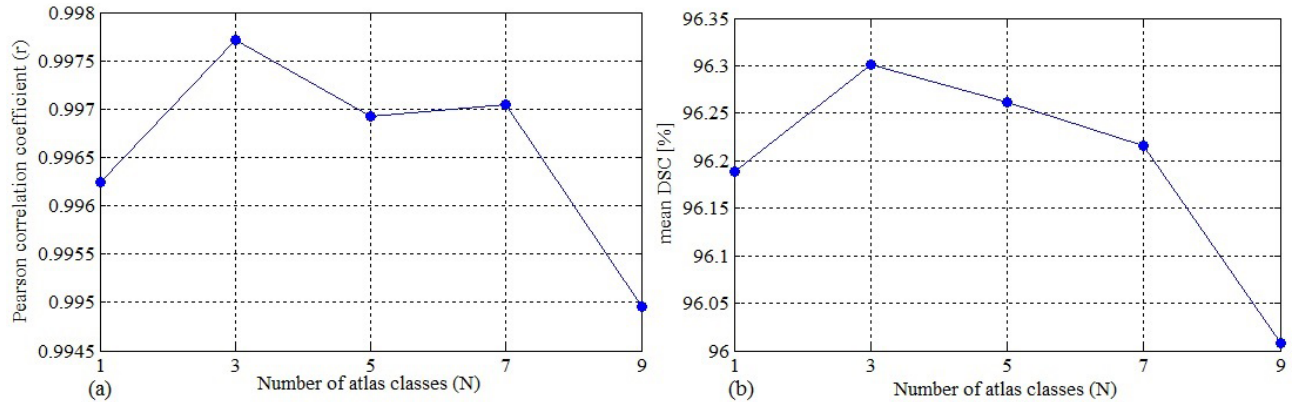
Figure 10. Finding the optimum value for the number of the atlas classes: a) Pearson correlation coefficient and b) mean DSC versus number of atlas classes.

pectoral muscle is considered in the breast area. The results exhibit that our implemented algorithm accurately segments the breast region for both simple and complex cases. However, the segmentation of breasts with fibroglandular tissue connected to the pectoral muscle still has minor FP and FN errors.

In Table 4, the average accuracies of the proposed segmentation method with and without the atlas-based refinement step are provided. As can be seen in this table, the atlas-based refinement step significantly influences the accuracy of the proposed segmentation method. Moreover, the average segmentation accuracies for different BI-RADS density categories are presented in this table. In this set, 11, 10, 10, and 11 cases for BI-RADS density groups I, II, III, and IV are available, respectively. For DSC and TO performance groups I and II outperform groups III and IV. The breasts of group I have the lowest FP and FN errors. Based on Table 4, the accuracy of the segmentation is almost the same for different BI-RADS density groups.

Table 4. The accuracy of the proposed segmentation method for the ACR BI-RADS density groups: mean (standard deviation).

		DSC (%)	TO (%)	FN (%)	FP (%)
Overall (42 cases) without atlas refinement		82.1 (9.4)	72.47 (13.8)	27.5 (13.8)	2.09 (1.5)
Overall (42 cases) with atlas refinement		96.46 (1.5)	96.41 (2)	3.59 (2)	3.51 (1.7)
BI-RADS density group with atlas refinement	I	97.37 (1)	96.9 (1.5)	3.1 (1.5)	2.12 (1)
	II	96.77 (1.5)	96.73 (2.3)	3.27 (2.3)	3.17 (1.4)
	III	96.11 (1.6)	96.2 (1.8)	3.8 (1.8)	3.99 (1.8)
	IV	95.63 (1.4)	95.83 (2.3)	4.17 (2.3)	4.62 (1.6)

Performance evaluation of the proposed segmentation method for the testing set is presented in Figure 12. The values of DSC, TO, FN, and FP metrics versus breast volume are shown in Figures 12a–12d, respectively. A larger breast volume results in higher DSC and TO and also lower FN and FP. The coefficient of determination (R^2) for linear regression between breast size and DSC, TO, FN, and FP is 0.495, 0.329, 0.329, and 0.319, respectively, noting that variation of breast size does not significantly influence the segmentation accuracy. Figure 13 demonstrates the case-based correlation between breast volume estimation from automatic and manual segmentations. The correlation coefficient (r) is 0.9983 with $R^2 = 0.996$ and $RMSE = 1.91\%$ which means a close accordance.
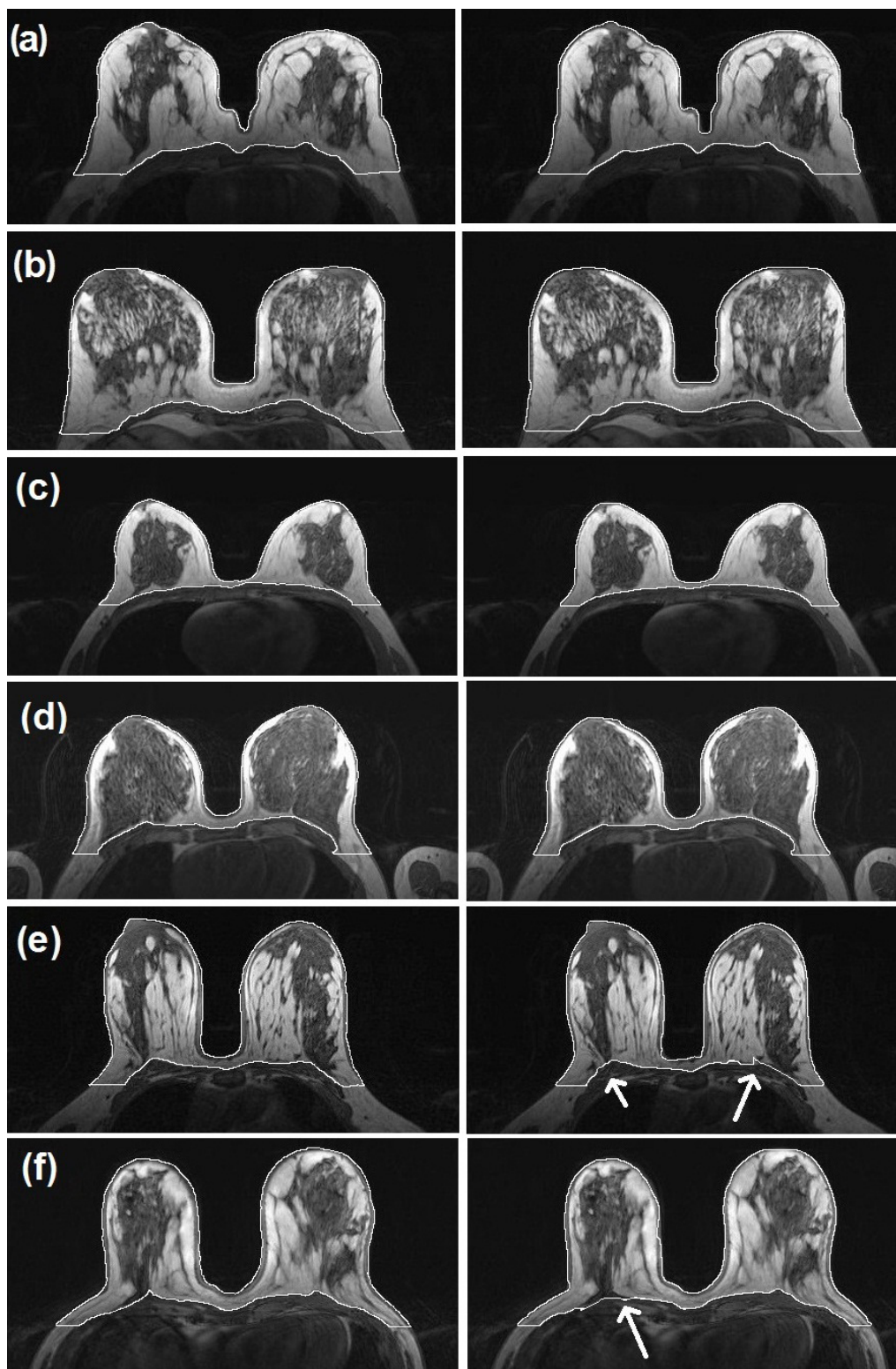
Figure 11. The manual and automatic segmentation results (first and second columns, respectively) for the selected breasts with simple cases (a, b), complex cases in which the breast region is accurately segmented with the proposed algorithm (c, d), complex case in which small parts of the breast region are incorrectly excluded by automatic segmentation algorithm (e), and complex case which small part of the pectoral muscle is considered in the breast area (f).
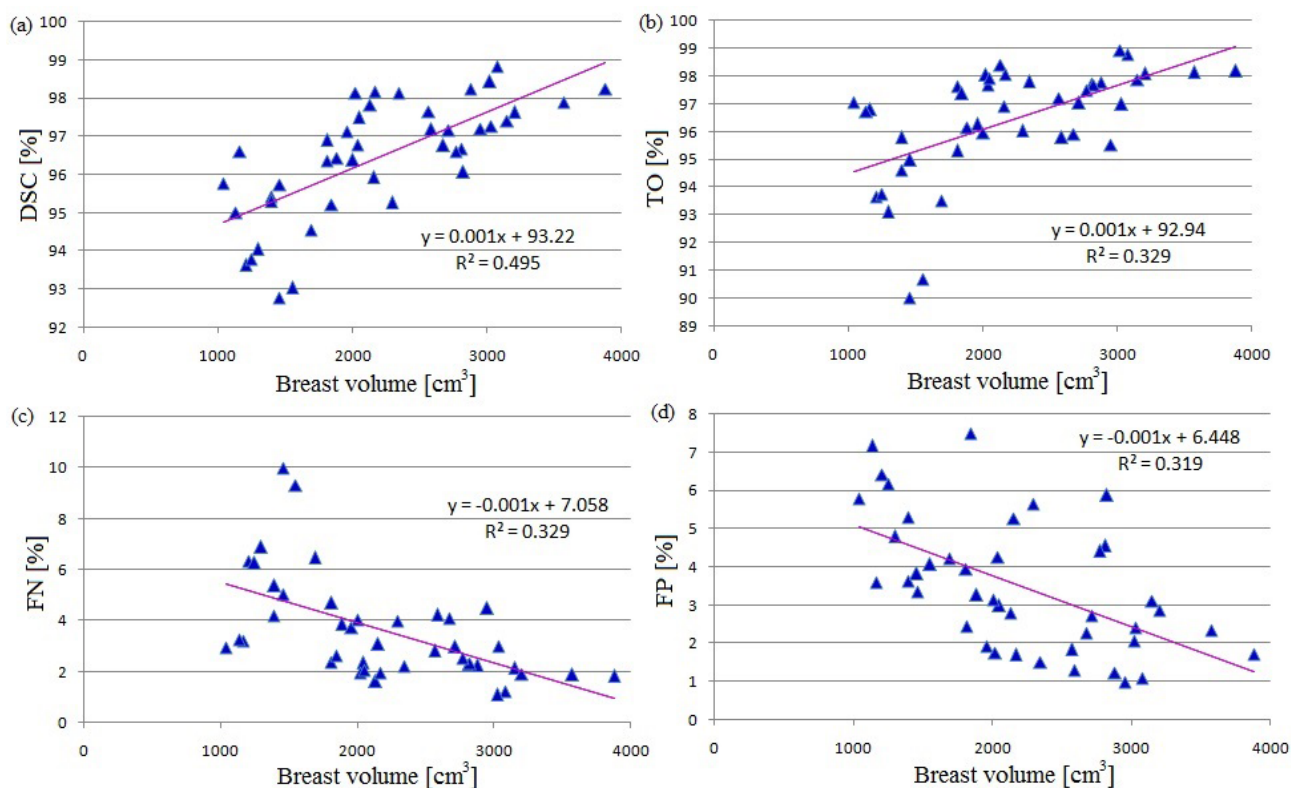
Figure 12. Performance evaluation of the proposed segmentation method versus breast volume: a) DSC, b) TO, c) FN, and d) FP.
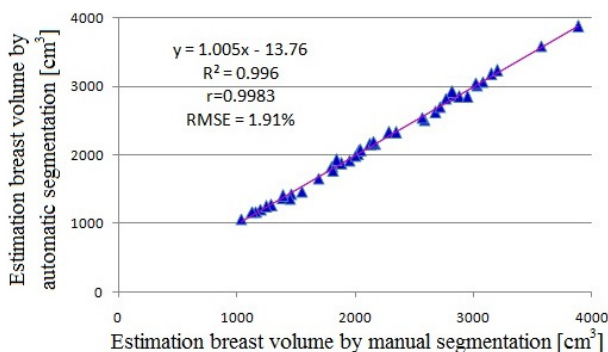

Figure 13. Case-based correlation between breast volume estimated from automatic and manual segmentations.

The values achieved by the validation metrics show the superiority of our approach in comparison with other breast MRI segmentation methods in the literature. The atlas-based method of Gubern-Mérida et al. [22] obtains DSC, TO, FP, and FN values of 94%, 96%, 7%, and 4% using a dataset of 27 cases. DSC, TO, FP, and FN values of 88%, 89%,13%, and 11% were reported in the work conducted by Gallego-Ortiz et al. [23]. They employed 409 MRI cases for validation of their algorithm, which is a larger set with respect to our collected dataset. Gallego-Ortiz et al. [23] and Lin et al. [16] illustrated examples and mentioned that their methods failed to detect the breast region for challenging cases. Furthermore, a number of challenging cases in their validation sets are not discussed. In our dataset, 68 out of 126 cases have fibroglandular tissues connected to the chest wall, and the remaining cases have diverse breast density. Among the mentioned methods, only

Milenković et al. [20] considered the breast segmentation issue for challenging cases and suggested a breast segmentation method independent from the contrast between the breast region and chest wall. Khalvati et al. [24], Wu et al. [15], and Milenković et al. [20] reported mean DSC values lower than that of the presented method. Quantitative comparison with several studies is not feasible, because they used different validation metrics [7,16] or did not report the accuracy of their proposed method [9–12]. It should also be noted that direct comparison between performances of different breast MRI segmentation methods is not very reliable as researchers mostly use different datasets, which comprise different manual annotations with a wide range of clinical imaging parameters.

4. Conclusions

Segmentation of the breast region is an initial stage for the diagnosis of breast cancer. A new combination algorithm of intensity-based and atlas-based methods is proposed, which is able to segment breasts with fibroglandular tissue connected to the chest wall. The presented approach is evaluated using the similarity between automatic and manual segmentation results. The segmentation accuracy of our method has been assessed using quality metrics such as DSC, TO, FN, and FP with the attained values of 96.46%, 96.41%, 3.59%, and 3.51%, respectively. Qualitative and quantitative results indicate that our method is relatively robust against variation of breast size and density.

Acknowledgment

References

[1] American Cancer Society. Breast Cancer Facts and Figures 2013–2014. Atlanta, GA, USA: American Cancer Society, 2014.

[2] Saslow D, Boetes C, Burke W, Harms S, Leach MO, Lehman CD, Morris E, Pisano E, Schnall M, Sener S et al. American Cancer Society guidelines for breast screening with MRI as an adjunct to mammography. CA-Cancer J Clin 2007; 57: 75-89.

[3] Behrens S, Laue H, Althaus M, Bohler T, Kuemmerlen B, Hahn HK, Peitgen HO. Computer assistance for MR based diagnosis of breast cancer: present and future challenges. Comput Med Imag Graph 2007; 31: 236-247.

[4] Wei J, Chan HP, Helvie MA, Roubidoux MA, Sahiner B, Hadjiiski LM, Zhou C, Paquerault S, Chenevert T, Goodsitt MM. Correlation between mammographic density and volumetric fibroglandular tissue estimated on breast MR images. Med Phys 2004; 31: 933-942.

[5] Nie K, Chen JH, Chan S, Chau MK, Yu HJ, Bahri S, Tseng T, Nalcioglu O, Su MY. Development of a quantitative method for analysis of breast density based on three-dimensional breast MRI. Med Phys 2008; 35: 5253-5262.

[6] Morris EA, Liberman L. Breast MRI: Diagnosis and Intervention. New York, NY, USA: Springer-Verlag, 2005.

[7] Ertas G, Gulcur HO, Osman O, Ucan ON, Tunaci M, Dursun M. Breast MR segmentation and lesion detection with cellular neural networks and 3D template matching. Comput Biol Med 2008; 38: 116-126.

[8] Ertas G, Doran SJ, Leach MO. A computerized volumetric segmentation method applicable to multi-centre MRI data to support computer-aided breast tissue analysis, density assessment and lesion localization. Med Biol Eng Comput 2017; 55: 57-68.

[9] Hayton P, Brady M, Tarassenko L, Moore N. Analysis of dynamic MR breast images using a model of contrast enhancement. Med Image Anal 1997; 1: 207-224.

[10] Yao J, Chen J, Chow C. Breast tumor analysis in dynamic contrast enhanced MRI using texture features and wavelet transform. IEEE J Sel Top Signal Process 2009; 3: 94-100.

[11] Twellmann T, Lichte O, Nattkemper TW. An adaptive tissue characterization network for model-free visualization of dynamic contrast-enhanced magnetic resonance image data. IEEE T Med Imaging 2005; 24: 1256-1266.

[12] Chen W, Giger ML, Lan L, Bick U. Computerized interpretation of breast MRI: investigation of enhancement-variance dynamics. Med Phys 2004; 31: 1076-1082.

[13] Shokouhi SB, Fooladivanda A, Ahmadinejad N. Computer-aided detection of breast lesions in DCE-MRI using region growing based on fuzzy C-means clustering and vesselness filter. EURASIP J Adv Signal Processing 2017; 39: 1-11.

[14] Giannini V, Vignati A, Morra L, Persano D, Brizzi D, Carbonaro L, Bert A, Sardanelli F, Regge D. A fully automatic algorithm for segmentation of the breasts in DCE-MR images. In: Proceedings of the 32nd Annual International Conference of the IEEE Engineering in Medicine and Biology Society; 31 August–4 September 2010; Buenos Aires, Argentina. New York, NY, USA: IEEE. pp. 3146-3149.

[15] Wu SD, Weinstein SP, Conant EF, Schnall MD, Kontos D. Automated chest wall line detection for whole-breast segmentation in sagittal breast MR images. Med Phys 2013; 40: 42301-42312.

[16] Lin M, Chen JH, Wang X, Chan S, Chen S, Su MY. Template-based automatic breast segmentation on MRI by excluding the chest region. Med Phys 2013; 40: 122301-122310.

[17] Wang L, Platel B, Ivanovskaya T, Harz M, Hahn HK. Fully automatic breast segmentation in 3D breast MRI. In: Proceedings of the IEEE International Symposium on Biomedical Imaging; 2012; New York, NY, USA: IEEE. pp. 1024-1027.

[18] Jiang L, Hu X, Xia Q, Gu Y, Li Q. Fully automated segmentation of whole breast using dynamic programming in dynamic contrast enhanced MR images. Med Phys 2017; 44: 2400-2414.

[19] Rosado-Toro JA, Barr T, Galons JP, Marron MT, Stopeck A, Thomson C, Thompson P, Carroll D, Wolf E, Altbach MI et al. Automated breast segmentation of fat and water MR images using dynamic programming. Acad Radiol 2015; 22: 139-148.

[20] Milenković J, Chambers O, Music MM, Tasic JF. Automated breast-region segmentation in the axial breast MR images. Comput Biol Med 2015; 62: 55-64.

[21] Rohlfing T, Brandt R, Menzel R, Russakoff DB, Maurer CR. Quo Vadis, atlas-based segmentation? In: Suri J, Wilson DL, Laxminarayan S, editors. The Handbook of Medical Image Analysis, Vol. III: Registration Models. New York, NY, USA: Kluwer Academic/Plenum Publishers, 2005. pp. 435-486.

[22] Gubern-Mérida A, Kallenberg M, Mann RM, Marti R, Karssemeijer N. Breast segmentation and density estimation in breast MRI: a fully automatic framework. IEEE J Biomed Health Inform 2015; 19: 349-357.

[23] Gallego-Ortiz C, Martel AL. Automatic atlas-based segmentation of the breast in MRI for 3D breast volume computation. Med Phys 2012; 39: 5835-5848.

[24] Khalvati F, Gallego-Ortiz C, Balasingham S, Martel AL. Automated segmentation of breast in 3-D MR images using a robust atlas. IEEE T Med Imaging 2015; 34: 116-125.

[25] Fooladivanda A, Shokouhi SB, Ahmadinejad N. Localized-atlas-based segmentation of breast MRI in a decision-making framework. Australas Phys Eng S 2017; 40: 69-84.

[26] Yushkevich PA, Piven J, Hazlett HC, Smith RG, Ho S, Gee JC, Gerig G. User-guided 3D active contour segmentation of anatomical structures: Significantly improved efficiency and reliability. NeuroImage 2006; 31: 1116-1128.

[27] Li C, Gore JC, Davatzikos C. Multiplicative intrinsic component optimization (MICO) for MRI bias field estimation and tissue segmentation. Magn Reson Imaging 2014; 32: 913-923.

[28] Sauvola J, Pietikainen M. Adaptive document image binarization. Pattern Recogn 2000; 33: 225-236.

[29] Haralick RM, Shapiro LG. Computer and Robot Vision. Boston, MA, USA: Addison-Wesley, 1992.

[30] Al Yousefi H, Udpa S. Recognition of Arabic characters. IEEE T Pattern Anal 1992; 14: 853-857.

[31] Soille P. Morphological Image Analysis: Principles and Applications. New York, NY, USA: Springer-Verlag, 1999.

[32] Chang DH, Chen JH, Lin M, Bahri S, Yu HJ, Mehta RS, Nie K, Hsiang DJB, Nalcioglu O, Su MY. Comparison of breast density measured on MR images acquired using fat-suppressed versus nonfat-suppressed sequences. Med Phys 2011; 38: 5961-5968.

[33] Abe S. Support Vector Machines for Pattern Classification. London, UK: Springer Verlag, 2005.

[34] Steyvers M. Multidimensional Scaling. Encyclopedia of Cognitive Science. New York, NY, USA: Wiley, 2006.

[35] Myronenko A, Song X. Intensity-based image registration by minimizing residual complexity. IEEE T Med Imaging 2010; 29: 1882-1891.

[36] Saki F, Tahmasbi A, Soltanian Zadeh H, Shokouhi SB. Fast opposite weight learning rules with application in breast cancer diagnosis. Comput Biol Med 2013; 43: 32-41.

[37] Verma B, McLeod P, Klevansky A. Classification of benign and malignant patterns in digital mammograms for the diagnosis of breast cancer. Exp Syst Appl 2010; 37: 3344-3351.

[38] Canu S, Grandvalet Y, Guigue V, Rakotomamonjy A. SVM and Kernel Methods MATLAB Toolbox. Rouen, France: INSA de Rouen, 2005.